



Full Length Article

Switching electrochromic performance improvement enabled by highly developed mesopores and oxygen vacancy defects of Fe-doped WO₃ films

Bon-Ryul Koo^a, Kue-Ho Kim^b, Hyo-Jin Ahn^{a,b,*}

^a Program of Materials Science & Engineering, Convergence Institute of Biomedical Engineering and Biomaterials, Seoul National University of Science and Technology, Seoul 01811, Republic of Korea

^b Department of Materials Science and Engineering, Seoul National University of Science and Technology, Seoul 01811, Republic of Korea



ARTICLE INFO

Keywords:

Fast-switching electrochromic performances
Fe-doped WO₃
Mesoporous structures
Oxygen vacancy defects
Sol-gel method
Camphene

ABSTRACT

In recent years, owing to the capability to reversibly adjust transparency, reflection, and color by the low electric field, electrochromic devices (ECDs) have received an extensive attention for their potential use in optoelectronic applications. However, considering that the performances of the ECDs, including coloration efficiency (CE, < 30.0 cm²/C) and switching speed (> 10.0 s), are still low for an effective applied use, critical efforts are needed to push the development of a unique nanostructure film to improve electrochromic (EC) performances. Specifically, as the large-scale applications (e.g. refrigerators, vehicles, and airplanes) of the ECDs have been recently developed, the study for improving switching speed is urgently needed for commercialization of the devices. In this context, the present study reports a novel nanostructure film of Fe-doped WO₃ films with highly developed mesopores and oxygen vacancy defects, fabricated using the Fe agent and the camphene-assisted sol-gel method. Fe-doped WO₃ films with highly developed mesopores and oxygen vacancy defects show remarkable EC performances with both fast switching speed (2.8 s for the coloration speed and 0.3 s for the bleaching speed) and high CE (71.1 cm²/C). These two aspects contribute to the synergistic effects of optimized Fe doping and camphene on the films and have outstanding values as compared to previously reported results of WO₃-based materials. Specifically, the fast switching speed is attributed to the shortened Li⁺ diffusion pathway of the highly developed mesopores; and the other is the improved electrical conductivity of the highly increased oxygen vacancy defects. In addition, the high CE value is due to an efficient charge transport as the result of a more effective electroactive contact of the morphology with highly developed mesopores, resulting in a large transmittance modulation with a small intercalated charge density.

1. Introduction

Today, with an increase of the need for energy-efficient and convenient environments in daily life, electrochromic devices (ECDs) have attracted extensive attention in terms of their promising applications, such as energy-save “smart window”, electronic displays, and adjustable mirrors [1–3]. These devices have many advantages, such as visibility in the sunlight, color variations, low operating voltage, and low memory effect; they can also reversibly and persistently vary transparency, color, or other optical properties (such as absorption and reflection) by the application of a small electric field, which is based on a change in the electronic structure of electrochromic (EC) materials as a result of electron-ion behavior [3,4]. The typical ECD structure consists of five superimposed layers: the two different EC layers, the ion conductor layer, and the two transparent conducting layers [5]. The EC layers are the most fundamental components in ECDs that strongly

dominate the EC performances of optical modulation, coloration efficiency (CE), and switching speed and can be classified into two types: cathodic materials (WO₃, MoO₃, and polythiophene derivative) coloring under ion intercalation and anodic materials (NiO, IrO₂, and polyaniline) coloring under ion deintercalation [6]. Specifically, an important parameter for the ECDs is the switching speed defined as the time required for electronic switching of light transmittance, absorption, and coloration [7]. However, as the ECDs exhibit a slow switching speed, more than 10.0 s for the full color transition, this can hinder commercialization of the devices. In addition, the switching speed is extremely slowed with the increase of the operating area in the devices (3.0–5.0 min for 1524 × 3048 mm² of SageGlass®) [8]. Therefore, further research seeking to improve the switching speed remains a critical issue for the development of the ECDs [9,10].

Due to the outstanding characterizations of harmlessness, low cost, good stability, and wide optical modulation among various EC

* Corresponding author at: Department of Materials Science and Engineering, Seoul National University of Science and Technology, Seoul 01811, Republic of Korea.
E-mail address: hjahn@seoultech.ac.kr (H.-J. Ahn).

materials, tungsten oxide (WO_3) corresponding to an indirect semiconductor with the band gap of 2.50–3.65 eV, has been conventionally used as one of the most representative cathodic EC materials in ECDs [11–13]. The WO_3 shows a reversible color change between the deep blue and the colorless by a response of the cathodic and anodic reaction. This phenomenon is attributed to intercalation/deintercalation of small protons ($\text{M} = \text{H}^+$, Na^+ , and Li^+) into WO_3 lattices (see Eq. (1)): [14]



Unfortunately, since CE ($< 30.0 \text{ m}^2/\text{C}$) and switching speed ($> 10.0 \text{ s}$) of the formed WO_3 film are relatively small, WO_3 is a critical limitation for the effective use in the applications. In particular, with recent advances in the development of large-scale applications (e.g. refrigerators, vehicles, and airplanes) using WO_3 -based ECDs, improving the switching speed of the devices has been highlighted as an important venue of future research and development. It is known that an increase of switching speed can be mainly achieved by strategies of 1-dimensional (D) and porous nanostructures and doping of metal ions [15–21]. First of all, the development of 1-D and porous nanostructures is useful in terms of enhancing switching speed due to providing a more effective contact area with electrolyte and reducing the diffusion length of ions during the EC reaction [22,23]. For example, using the hydrothermal method, Ma et al. synthesized vertically aligned 1-D WO_3 films that showed a faster switching speed (6.7 s for the coloration speed and 3.4 s for the bleaching speed) as compared to those of the bare nanorod WO_3 films [22]. Furthermore, Cronin et al. demonstrated that the porous WO_3 films prepared by the dip coating method at the optimum viscosity of dipping solutions showed an improved switching speed (37.0 s for the coloration speed and 5.0 s for the bleaching speed) as compared to that of the dense WO_3 films [23]. In addition, the doping of metal ions such as Ni into WO_3 lattices were reported to be able to enhance the switching speed by the reduced charge transfer resistance [24,25]. Using the hydrothermal method, Zhou et al. prepared Ni-doped WO_3 films and their results indicated that the 0.5% Ni doping could have an enhanced switching speed (7.8 s for the coloration speed and 6.0 s for the bleaching speed) as compared to those of bare WO_3 films [24]. Yet, despite these efforts, the implementation of fast switching speed below 1.0 s has yet been limited for WO_3 -based ECDs. Hence, in the present study, we applied a novel way to obtain the fast switching speed of WO_3 -based films by both Fe doping and highly developed mesopores.

In the present study, we report a novel nanostructure film of Fe-doped WO_3 films with highly developed mesopores and oxygen vacancy defects using the Fe agent and the camphene-assisted sol-gel method. The Fe agent and camphene play a particularly attractive role causing the nanostructure film with highly developed mesopores and oxygen vacancy defect on the WO_3 , resulting in an impressive improvement of their EC performances, including both fast switching speed below 1.0 s and high CE.

2. Experiments

Fe-doped WO_3 films with highly developed mesopores and oxygen vacancy defects were prepared by the spin-coating sol solution with both Fe agent and camphene on a commercial FTO glass (Pilkington, $8.0 \Omega/\square$). For the preparation of the sol solution, tungsten (VI) chloride (WCl_6 , Aldrich) and iron (III) nitrate nonhydrate ($\text{Fe}(\text{NO}_3)_3 \cdot 9\text{H}_2\text{O}$, Aldrich) as the agent for Fe doping were dissolved in 2-propanol ($(\text{CH}_3)_2\text{CHOH}$, Aldrich), in which amount of Fe/W varied to be 3, 5, and 7 at% to optimize the EC performances of the Fe-doped WO_3 films. Thereafter, in order to obtain the Fe-doped WO_3 films with highly developed mesopores and oxygen vacancy defects, 10 wt% camphene (Hill Notation) $\text{C}_{10}\text{H}_{16}$, Aldrich) as the organic additive to the solvent were added into the sol solutions with 5 at% Fe as an optimized condition. After stirring for 3 h at room temperature, the resultant solutions

were deposited on the commercial FTO glass using the spin coating method, which was performed at 2000 rpm for 30 s and then repeated 2 times. In the next step, the samples were annealed at 300°C in air to form the Fe-doped WO_3 films with highly developed mesopores and oxygen vacancy defects. For comparison, bare WO_3 films and Fe-doped WO_3 films were fabricated by spin-coating the WCl_6 sol solution without additive and with the amount of 3, 5, and 7 at% Fe. Therefore, we obtained five types of bare WO_3 films, Fe-doped WO_3 films with 3, 5, and 7 at% Fe, and Fe-doped WO_3 films using camphene with 5 at% Fe. The obtained films were marked as bare WO_3 , 3Fe- WO_3 , 5Fe- WO_3 , 7Fe- WO_3 , and CFe- WO_3 , respectively.

The thermal behaviour of the samples was identified by differential scanning calorimetry (DSC, DSC-60, Shimadzu). The surface morphology was investigated using a field-emission scanning electron microscopy (FESEM, Hitachi S-4800) and an atomic force microscopy (AFM, diDimensionTM 3100). The crystal structure and chemical state were investigated by X-ray diffraction (XRD, Rigaku D/Max-2500 diffractometer using Cu K_α radiation) and X-ray photoelectron spectroscopy (XPS, AXIS ultra-delay line detector equipped with an Al K_α X-ray source, KBSI Daedeok Headquarters), respectively. The electrical and optical properties were analyzed by a Hall-effect measurement system (Ecopia, HMS-3000) and ultraviolet-visible (UV-vis) spectroscopy (Perkim-Elmer, Lambda-35), respectively. The electrochemical and EC performances were characterized using a potentiostat/galvanostat (PGSTAT302N, FRA32M, Metrohm Autolab B.V., the Netherlands) in a three-electrode electrochemical cell with 1 M LiClO_4 as the electrolyte, Pt wire as the counter electrode, and Ag wire as the reference electrode. *In situ* optical properties related to switching speed were measured using ultraviolet-visible (UV-vis) spectroscopy (Perkim-Elmer, Lambda-35) in the wavelength at 633 nm.

3. Results and discussion

We constructed the Fe-doped WO_3 films with highly developed mesopores and oxygen vacancy defects through the sol-gel method using Fe dopant and camphene. To trace the formation behavior of the highly developed mesopore on the films, the thermal analysis on the sol solutions for forming bare WO_3 , 5Fe- WO_3 , and CFe- WO_3 using DSC was performed under air in the range of $25\text{--}300^\circ\text{C}$ (see Fig. 1a). All samples mainly included two major stages at $25\text{--}75^\circ\text{C}$ and $115\text{--}135^\circ\text{C}$. The rapid endothermic peak observed at $25\text{--}75^\circ\text{C}$ was due to the elimination of the solvent in the samples. The major endothermic peak from 115 to 135°C could be attributed to the hydrolysis of WCl_6 related to formation of the WO_3 [26]. For 5Fe- WO_3 , there was an extra endothermic peak at $95\text{--}115^\circ\text{C}$ induced by thermal decomposition of the $\text{Fe}(\text{NO}_3)_3 \cdot 9\text{H}_2\text{O}$ for Fe doping into WO_3 lattices [27]. Furthermore, CFe- WO_3 showed a broad endothermic peak at $84\text{--}115^\circ\text{C}$. This included two major peaks of the thermal decompositions related to camphene at $84\text{--}102^\circ\text{C}$ and $\text{Fe}(\text{NO}_3)_3 \cdot 9\text{H}_2\text{O}$ at $95\text{--}105^\circ\text{C}$ [28]. These DSC results demonstrate the formation behavior of the nanostructure film with highly developed mesopores (CFe- WO_3) (see Fig. 1b). During the annealing process, the critical two steps were generated by the thermal decomposition of the camphene and the Fe agent. In the first step (centered at 95°C), the thermal decomposition of the camphene could cause the partial Kirkendall effect of W^{6+} electrostatic-interacted with isobornyl alkyl ether converted by camphene and 2-propanol, which was due to a higher diffusion coefficient of the camphene ($D = 12 \times 10^{-8} \text{ m}^2\text{s}^{-1}$) than that of pure W^{6+} ($D = 70 \times 10^{-8} \text{ m}^2\text{s}^{-1}$) [28,29], resulting in the formation of the mesopores with the average diameter of 23.2 nm on the WO_3 films. In the second step (centered at 105°C), Fe doping into WO_3 could result in the distortion of the WO_3 structure due to a mismatch (0.02 \AA) of the ionic radius between Fe^{3+} (0.64 \AA) and W^{6+} (0.62 \AA) [29,30], which could form the mesopores with the average diameter of 35.9 nm [31]. The resultant nanostructure film consisted of the highly developed mesopores with the two different average diameters of 23.2 nm and 35.9 nm by the synergistic effect of

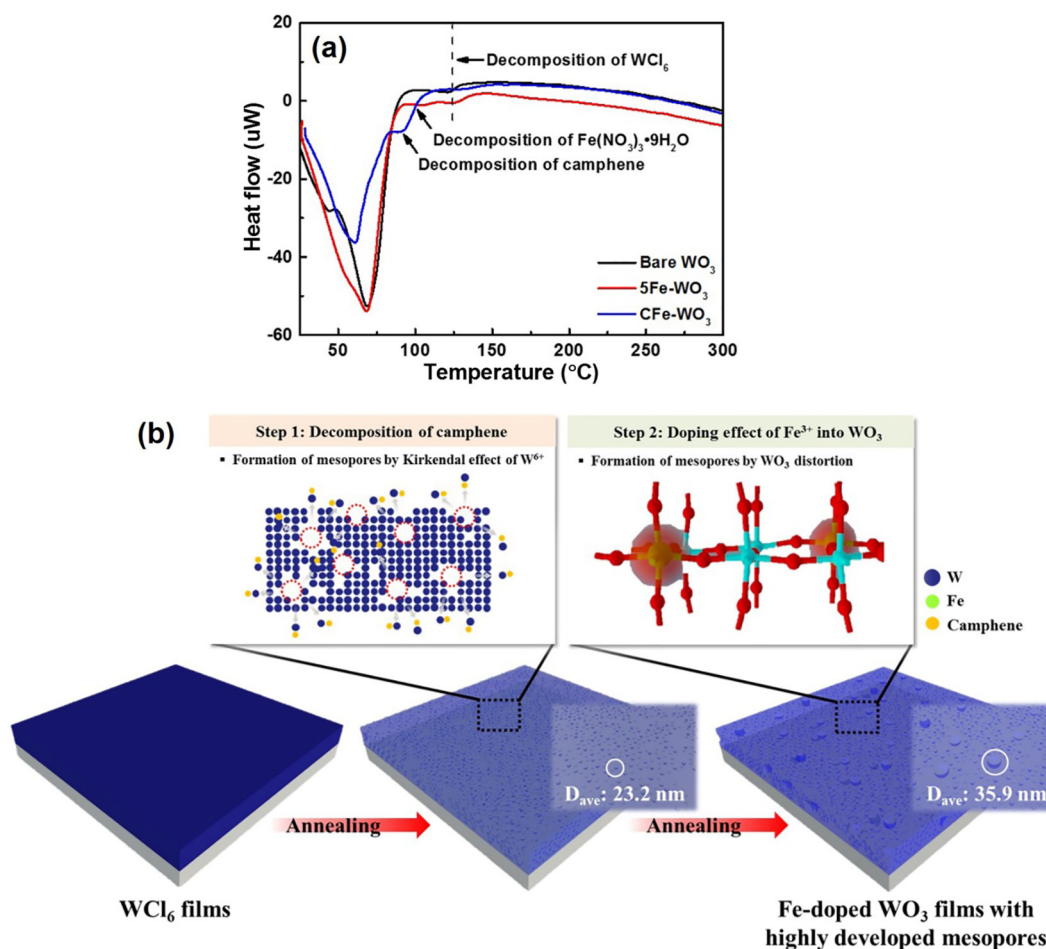


Fig. 1. (a) DSC curves of bare WO_3 , 5Fe-WO_3 , and CFe-WO_3 in range of 25–300 °C at air atmosphere and (b) schematic illustration for formation behavior of the film structure with highly developed mesopores during annealing process.

camphene and Fe doping, thus resulting in the formation of the nanostructure film with highly developed mesopores to improve the EC performances.

Fig. 2a–e shows top-view FESEM images of bare WO_3 , 3Fe-WO_3 , 5Fe-WO_3 , 7Fe-WO_3 , and CFe-WO_3 , respectively. Specifically, bare WO_3 (see Fig. 2a) had a smooth surface morphology consisting of densely packed nanoparticles with the diameter of 8.1–12.1 nm. On the other hand, the Fe-doped WO_3 films (see Fig. 2b,c) showed the mesoporous surface morphology, where the size and distribution of the mesopores gradually enhanced with an increase of the amount of Fe from 3 at% (Fig. 2b: 8.6–24.3 nm in diameter) to 5 at% (Fig. 2c: 31.4–44.2 nm in diameter) due to the effect of Fe doping into WO_3 lattices. According to Zhou et al., doping of metal ions leads to a disorder in the WO_3 structure and their disorder degree increases with an increase of the amount of metal doping [24]. However, when the amount of Fe reaches 7 at%, the decreased size and distribution of the mesopores are observed, which is due to the formation of aggregation by an excessive amount of Fe (see Fig. 2d). Interestingly, for CFe-WO_3 , the highly developed mesopores with the diameter of two different scales (17.5–29.2 and 32.8–49.1 nm) were simultaneously observed on the surface, indicating that little small mesopores (17.5–29.2 nm in diameter) were formed among the relatively large mesopores (32.8–49.1 nm in diameter) caused by the distortion by Fe doping, due to the Kirkendall effect of camphene [32,33], as suggested by the mesopore diameter distribution in Fig. 3. Therefore, the synergistic effect of Fe doping and camphene on the WO_3 films can cause the formation of the nanostructure film with highly developed mesopores, which can be useful for the improvement of the surface area related to the electrostatic contact with

the electrolyte, as confirmed by the highest root mean square roughness (R_{ms}) among the samples (9.3 nm for bare WO_3 , 20.3 nm for 5Fe-WO_3 , and 32.0 nm for CFe-WO_3) shown in the AFM results (see Fig. S1a–c). In addition, the thicknesses of the samples amounted to 177.2–199.9 nm for bare WO_3 , 176.8–199.9 nm for 3Fe-WO_3 , 178.4–201.8 nm for 5Fe-WO_3 , 177.0–200.6 nm for 7Fe-WO_3 , and 178.7–201.1 nm for CFe-WO_3 (see Fig. S2), indicating that, without the influence of Fe doping and camphene, all samples had similar thickness values. Therefore, as suggested by the SEM and AFM results, CFe-WO_3 exhibited more highly developed mesopores as compared to other samples, which can facilitate increasing the electroactive contact between the electrode and the electrolyte and shorten the ion diffusion to improve the EC performances such as switching speeds and CE [34].

Fig. 4a shows the XRD curve obtained from all samples. A broad diffraction peak emitted at 23.1° is in agreement with the XRD pattern of amorphous WO_3 structure that is valuable to the EC performances due to its loose structure that facilitates fast ion diffusion [35]. However, no apparent peaks related to Fe were detected in the samples with Fe. To characterize the chemical binding states of the samples, we conducted the XPS measurements (see Fig. 4b,c). The values of all binding energies were determined by fixing the C 1s to the binding energy of 284.5 eV. In W 4f XPS core-level spectra (see Fig. 4b), bare WO_3 had one pair of doublets at 35.1 eV for W $4f_{7/2}$ and 37.2 eV for W $4f_{5/2}$, which was assigned to the binding energy of W^{6+} . On the other hand, for other samples, two pairs of doublets for W 4f were emitted; the lower-energy peaks at 34.5 eV for W $4f_{7/2}$ and 36.5 eV for W $4f_{5/2}$ indicating the binding energy of W^{5+} and the higher-energy peaks at 35.1 eV for W $4f_{7/2}$ and 37.2 eV for W $4f_{5/2}$ corresponding to that of

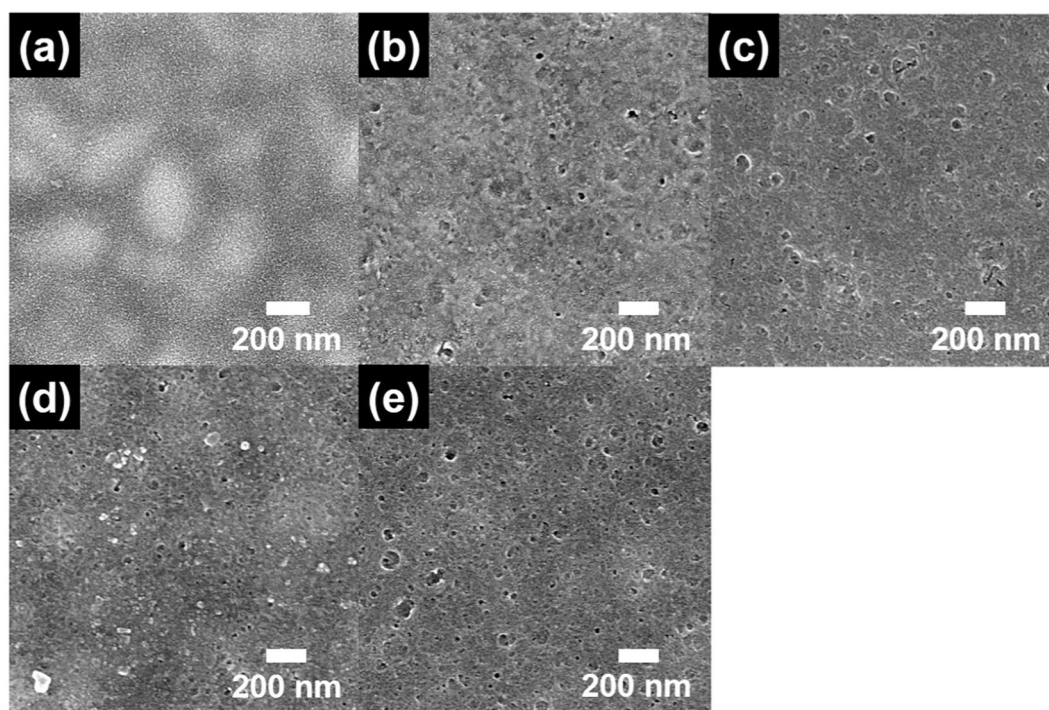


Fig. 2. Top-view FESEM images obtained from (a) bare WO_3 , (b) 3Fe-WO_3 , (c) 5Fe-WO_3 , (d) 7Fe-WO_3 , and (e) CFe-WO_3 .

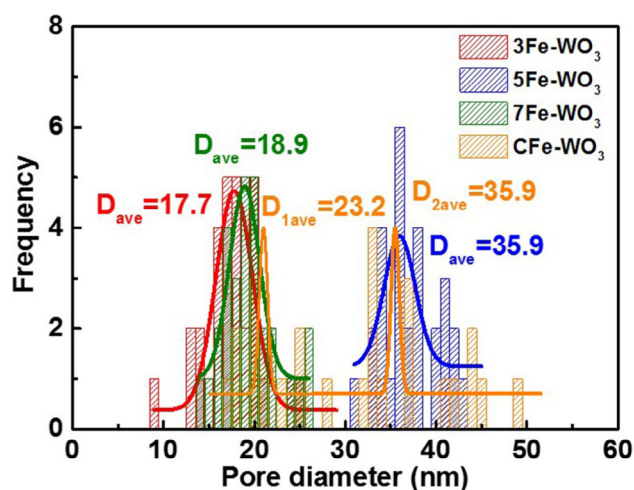


Fig. 3. Distribution of pore diameter for 3Fe-WO_3 , 5Fe-WO_3 , 7Fe-WO_3 , and CFe-WO_3 .

W^{6+} . These results suggest the emergence of oxygen vacancy defects as a result of the formation of the Fe-doped WO_3 phase by Fe^{3+} substitution at W^{6+} sites [36]. This result can lead to the formation of two electrons by the interaction of Fe dopant and associated oxygen vacancies, as well as to an effective electron transport by a continuous lattice structure so that oxygen ion neighbors oxygen vacancies, which can affect the electrical conductivity and optical bandgap of the samples, ultimately improving the EC performances [4,37]. Interestingly, the area ratios of $\text{W}^{5+}/\text{W}^{6+}$ peaks gradually increased from 7.0% for 3Fe-WO_3 to 11.0% for 5Fe-WO_3 . This was attributed to the increased number of oxygen vacancy defects with the increase of Fe doping level on the WO_3 [38]. For 7Fe-WO_3 , a decreased area ratio of $\text{W}^{5+}/\text{W}^{6+}$ (8.0%) was observed, which was due to the Fe_2O_3 phase (Fe–O bond) formed by excessive amount of Fe shown in O 1s XPS core-level spectra (see Fig. 4c) [29]. This was also proved by the advent of W^{4+} (33.5 eV) induced by the reduction for forming Fe_2O_3 [39,40], as shown in W 4f

XPS core-level spectra (see Fig. 4b). In particular, CFe-WO_3 showed an extremely large value of $\text{W}^{5+}/\text{W}^{6+}$ area ratio (16.0%), indicating that this sample possessed a much higher number of oxygen vacancy defects than the other samples. To further confirm the degree of oxygen vacancy defects on the samples, we investigated the atomic ratio of O/W based on W 4f and O 1s XPS core-level spectra: 3.06 for bare WO_3 , 2.90 for 3Fe-WO_3 , 2.84 for 5Fe-WO_3 , 2.87 for 7Fe-WO_3 , and 2.75 for CFe-WO_3 (see Fig. 4d). The obtained results indicated that the synergistic effect of Fe doping and camphene can lead to highly increased oxygen vacancy defects, in which the camphene can act as a reducing agent to capture the oxygen of metal oxide by carbothermic reaction, thus causing the improved electrical conductivity among the samples due to the increased oxygen vacancy defects (see Fig. S3a) [41]. With an increase of the amount of Fe, due to the upshift of valence band maximum (VBM) and downshift of conduction band minimum (CBM) by the hybridization between the Fe 3d orbital and the O 2p orbital [34], the optical bandgap was observed to gradually decrease from 2.74 eV for bare WO_3 to 2.64 eV for 5Fe-WO_3 (see Fig. S3b). When the amount of Fe reached 7 at%, optical bandgap rapidly decreased (2.42 eV), resulting from the formation of the Fe_2O_3 phases with the small optical bandgap of 2.0–2.2 eV [42]. Therefore, the nanostructure film with both highly developed mesopores and oxygen vacancy defects can directly affect the EC performances such as switching speeds and CE [43,44].

To characterize the electrochemical reaction of the samples during the electrochromic process (intercalation and deintercalation of Li^+), the CV analyses were performed in the three-electrode system with 1 M LiClO_4 as the electrolyte, Ag wire as the reference electrode, and Pt wire as the counter electrode in the potential region of -0.7 to 1.0 V (vs. Ag wire) at the scan rate of 20 mV/s. During the CV cycling, the color variation of the samples was reversibly caused from deep blue (colored state) to transparent (bleached state) as a result of the intercalation/deintercalation of Li^+ into/out of the samples. As can be seen in Fig. 5a, both anodic and cathodic current densities of the Fe-doped WO_3 samples were larger than those of bare WO_3 ; thereafter, they increased with an increase of the amount of Fe from 3 to 5 at% and then decreased when the amount of Fe amounted to 7 at%. Furthermore, for CFe-WO_3 , the largest current densities were observed, as compared to the other

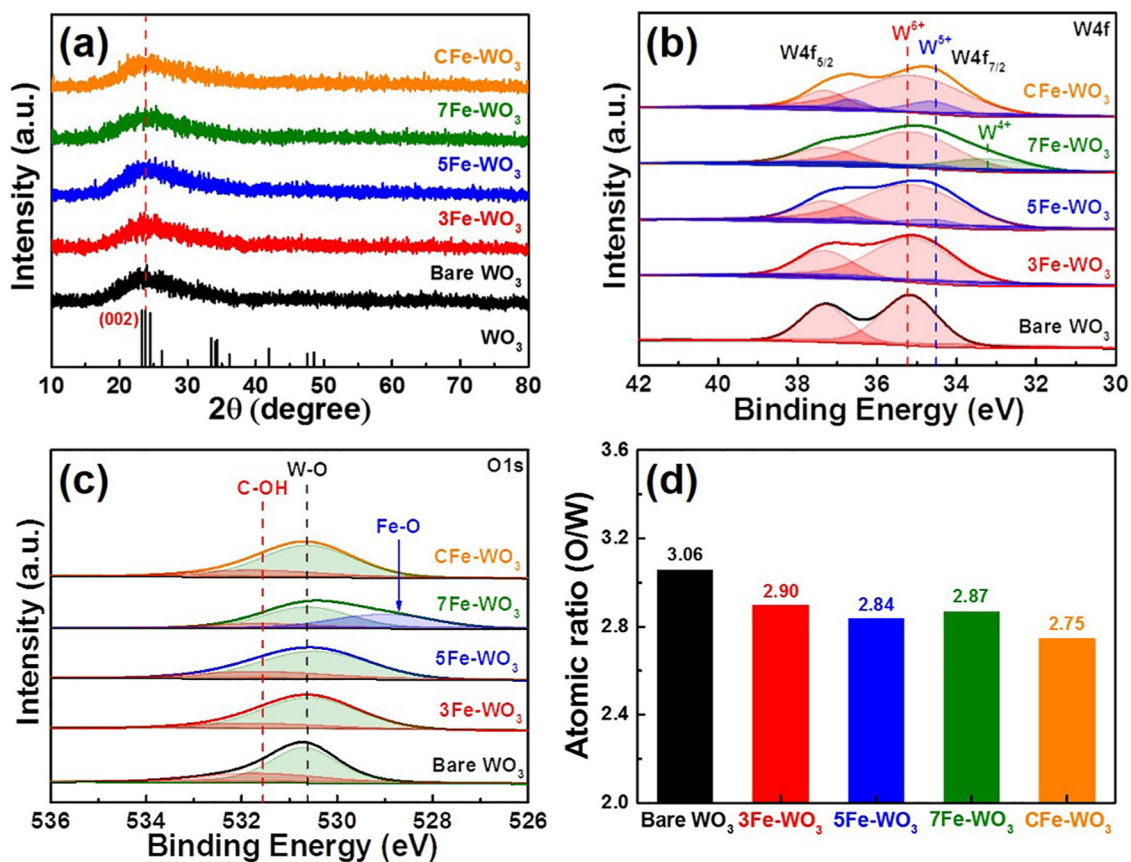


Fig. 4. (a) XRD curves, XPS core-level spectra of (b) W 4f and (c) O 1s, and (d) variation of O/W atomic ratio for all samples.

samples. This larger current density signifies the increase in number of ions and electrons to diffuse and transfer into or out the samples, indicating an enhancement of the electrochemical activity related to the EC performances [16]. Therefore, we estimated the diffusion coefficient (D) of the Li^+ on the samples using the Randles–Sevcik equation (see Eq. (2)) [45,46]:

$$J_p = 2.72 \times 10^5 \times D^{1/2} \times C_o \times \nu^{1/2} \quad (2)$$

where J_p is the peak current density, C_o is the concentration of active ions in the solution, and ν is the sweep rate. As shown in Table 1, with the function of the amount of Fe, due to the increased oxygen vacancy defects resulting from an accelerated effect of Fe doping, the diffusion coefficient increased from $0.25 \times 10^{-8} \text{ cm}^2/\text{s}$ for bare WO_3 to $1.06 \times 10^{-8} \text{ cm}^2/\text{s}$ for 5Fe-WO_3 . However, 7Fe-WO_3 showed the decreased diffusion coefficient ($0.34 \times 10^{-8} \text{ cm}^2/\text{s}$) as compared to 5Fe-WO_3 despite a high amount of Fe doping, stemming from the decreased effect of the Fe doping due to the Fe_2O_3 aggregates by an excessive amount of Fe. In particular, CFe-WO_3 exhibited a highly fasted diffusion coefficient ($1.49 \times 10^{-8} \text{ cm}^2/\text{s}$) that was nearly 5.96 times higher than that of bare WO_3 . Such diffusion coefficient is related to the highly increased oxygen vacancy defects by the synergistic effect of Fe doping and camphene in the films, which was also proved by the value of their electrical conductivity (see Fig. S3a). To trace the EC responses of the samples during switching, the *in situ* optical transmittances at colored and bleached states of the devices were monitored as a function of time at $\lambda_{633\text{nm}}$ by applying the potential of -0.7 (colored state) and 1.0 V (bleached state) for 60 s, respectively. From the obtained curve (see Fig. 5b), the transmittance modulation (defined as $\Delta T = T_b - T_c$, where T_b is transmittance in the bleached state and T_c is transmittance in the colored state) and switching speed (defined as the time to reach 90% of the entire transmittance modulation at 633 nm) were determined (see Table 1 for a summary). Due to a decreased transmittance

in the bleached state by narrowing the optical band gap as an effect of Fe doping into WO_3 , the transmittance modulation of the Fe-doped WO_3 samples exhibited slightly decreased values as compared to those of bare WO_3 . For CFe-WO_3 , their transmittance modulation was revealed to possess a higher value (53.0%) than that of 5Fe-WO_3 (51.1%), which can be attributed to the decreased transmittance in the colored state by the increased Li^+ intercalation capacity due to the highly developed mesopores, thus showing the implementation of deep-blue color on CFe-WO_3 compared to bare WO_3 and 5Fe-WO_3 (see Fig. S4). Interestingly, with an increase of the amount of Fe from 0 at% (11.7 s for the coloration speed and 14.6 s for the bleaching speed) to 5 at% (7.2 s for the coloration speed and 2.2 s for the bleaching speed), the switching speeds improved, which was due to the increased mesopores at surface and the improved electrical conductivity caused from the effect of Fe doping, resulting in the reduction of Li^+ diffusion pathway and the acceleration of the Li^+ and electron diffusion during intercalation/deintercalation processes [24,25]. Due to the reduction effect of the mesopores and electrical conductivity resulting from the formation of the Fe_2O_3 aggregates, the observed switching speeds of 7Fe-WO_3 were slow (11.8 s for the coloration speed and 8.0 s for the bleaching speed). Surprisingly, CFe-WO_3 exhibited the fastest switching speeds (2.8 s for the coloration speed and 0.3 s for the bleaching speed) as compared to those of the other samples in our study and many other WO_3 -based materials reported previously (see Table S1), which is a remarkable result in terms of enhancing the EC performance of fast switching speed in accordance with a value below 1.0 sec despite WO_3 -based materials [47,48]. This attractive performance is due to the novel nanostructure film of the Fe-doped WO_3 film with highly developed mesopores and oxygen vacancy defects caused by Fe doping and camphene, which can facilitate the intercalation/deintercalation processes of Li^+ by offering the shortened diffusion pathway and increased electrical conductivity on the WO_3 . In addition, the CE, defined as the

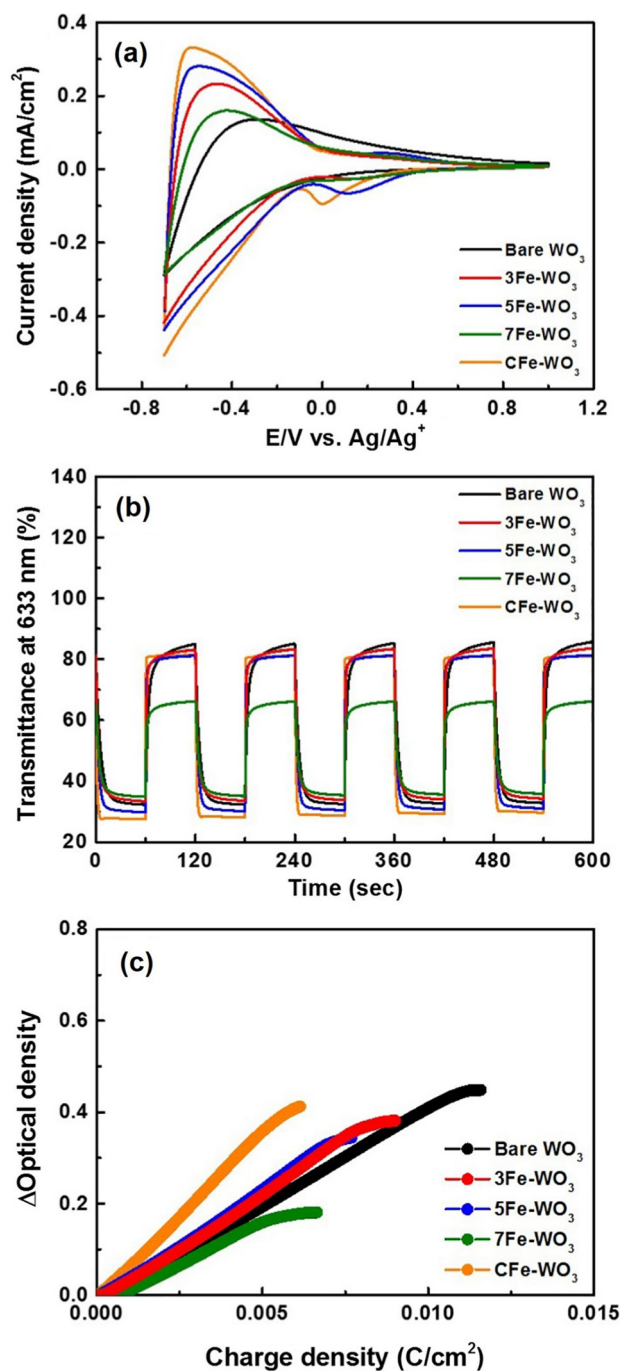


Fig. 5. (a) CV curves of the samples measured in the potential range of -0.7 to 1.0 V at scan rate of 20 mV/s using a three-electrode system, (b) *In situ* optical transmittances measured by applying the potential of -0.7 (colored state) and 1.0 V (bleached state) for 60 s, and (c) variation of OD as a function of intercalated charge density at 633 nm.

Table 1

Summary of electrochromic properties obtained from all samples.

Samples	T_b (%)	T_c (%)	Transmittance modulation (%)	Coloration speed (s)	Bleaching speed (s)	CE (cm^2/C)
Bare WO_3	85.0	32.2	52.8	11.7	14.6	35.9
3Fe- WO_3	83.0	33.5	49.5	9.0	4.4	43.7
5Fe- WO_3	81.2	30.1	51.1	7.2	2.2	46.2
7Fe- WO_3	66.2	35.0	31.2	11.8	8.0	31.8
CFe- WO_3	81.3	28.3	53.0	2.8	0.3	71.1

change in the optical density (OD) per unit intercalated charge densities (Q/A), is one of the most important factors to determine the high-performance EC materials. It can be calculated as shown in Eqs. (3) and (4) [3]:

$$\text{CE} = \Delta\text{OD}/(Q/A) \quad (3)$$

$$\Delta\text{OD} = \log(T_b/T_c) \quad (4)$$

where Q and A are the integration of the current within the colored time and the given electrode area, respectively; a high value of the CE means that the CE materials offer a large transmittance modulation with a small charge density. Fig. 5c shows the curve of OD as a function of intercalated charge density at the wavelength of 633 nm. When the potential of -0.7 V was applied to the samples, CE values were 35.9 cm^2/C for bare WO_3 , 43.7 cm^2/C for 3Fe- WO_3 , 46.2 cm^2/C for 5Fe- WO_3 , 31.8 cm^2/C for 7Fe- WO_3 , and 71.1 cm^2/C for CFe- WO_3 . Therefore, CFe- WO_3 exhibited a superb CE value as compared to the other samples. Therefore, we achieved noticeable fast switching speeds and high CE value for the EC devices by constructing the Fe-doped WO_3 films with highly developed mesopores and oxygen vacancy defects as the novel film structure, which could be mainly attributed to the synergistic effects of optimized Fe doping and camphene on the films. First, the remarkably fast switching speed (2.8 s for the coloration speed and 0.3 s for the bleaching speed) was due to the combined effects of reducing the Li^+ diffusion pathway by highly developed mesopores consisting of two different average mesopore sizes (23.2 nm from camphene and 35.9 nm from Fe doping) and enhancing electrical conductivity by highly increased oxygen vacancy defects caused from the Fe doping and camphene. Second, the superior CE (71.1 cm^2/C) was induced by the improvement of an efficient charge transport by a more effective electroactive contact due to highly developed mesopores, leading to a large transmittance modulation with respect to a small intercalated charge density.

4. Conclusions

In the present study, Fe-doped WO_3 films with highly developed mesopores and oxygen vacancy defects were successfully prepared by using the Fe agent and the camphene-assisted sol-gel method. By varying the amount of Fe in the WO_3 , we demonstrated that the optimized effect of Fe doping (5 at% Fe) into the WO_3 can form the surface morphology with mesopores of the diameter of 32.8 – 49.1 nm due to both WO_3 distortion and oxygen vacancy defects by the Fe^{3+} substitution at W^{6+} sites. Furthermore, camphene used as the organic additive was found to play a functional role accelerating both mesopores with the diameter of 17.5 – 29.2 nm and oxygen vacancy defects as induced by their Kirkendall effect of W^{6+} and carbothermic reaction, respectively. Therefore, the Fe-doped WO_3 films with highly developed mesopores and oxygen vacancy defects (CFe- WO_3) showed noticeable EC performances, including both fast switching speed (2.8 s for the coloration speed and 0.3 s for the bleaching speed) and high CE (71.1 cm^2/C). Specifically, the fast switching speed in our study showed a superior value as compared to previously reported results on WO_3 -based films. These noticeable EC performances can be attributed to the synergistic effects of optimized Fe doping and camphene on the films; the remarkable fast switching speeds were due to the shortened Li^+ diffusion pathway by highly developed mesopores and the improved electrical conductivity by highly increased oxygen vacancy defects. In addition, the high CE value was intimately related to a more effective electroactive contact of highly developed mesopores providing an efficient charge transport, which resulted in a large transmittance modulation with respect to a small intercalated charge density. Taken together, the results of the present study provide a novel sight in nanostructure films to obtain the fast electrochromic performances for practical applications of WO_3 -based ECDs.

Acknowledgement

This research was supported by Basic Science Research Program through the National Research Foundation of Korea (NRF) funded by the Ministry of Science, ICT and Future Planning (NRF-2015R1A1A1A05001252).

Appendix A. Supplementary material

Supplementary data associated with this article can be found, in the online version, at <https://doi.org/10.1016/j.apsusc.2018.05.094>.

References

- [1] H. Li, J. Wang, Q. Shi, M. Zhang, C. Hou, G. Shi, H. Wang, Q. Zhang, Y. Li, Q. Chi, Constructing three-dimensional quasi-vertical nanosheet architectures from self-assemble two-dimensional $\text{WO}_3 \cdot 2\text{H}_2\text{O}$ for efficient electrochromic devices, *Appl. Surf. Sci.* 9 (2017) 281–287.
- [2] X. Chang, R. Hu, S. Sun, J. Liu, Y. Lei, T. Liu, L. Dong, Y. Yin, Sunlight-charged electrochromic battery based on hybrid film of tungsten oxide and polyaniline, *Appl. Surf. Sci.* 441 (2018) 105–112.
- [3] Y. Yin, C. Lan, H. Guo, C. Li, Reactive sputter deposition of $\text{WO}_3/\text{Ag}/\text{WO}_3$ film for indium tin oxide (ITO)-free electrochromic devices, *ACS. Appl. Mater. Interfaces* 8 (2016) 3861–3867.
- [4] B.-R. Koo, H.-J. Ahn, Fast-switching Electrochromic properties of mesoporous WO_3 films with oxygen vacancy defects, *Nanoscale* 9 (2017) 17788–17793.
- [5] G. Cai, J. Wang, P.S. Lee, Next-generation multifunctional electrochromic devices, *Acc. Chem. Res.* 49 (2016) 1469–1476.
- [6] S. Liu, X. Qu, Construction of nanocomposite film of Dawson-type polyoxometalate and TiO_2 nanowires for electrochromic applications, *Appl. Surf. Sci.* 412 (2017) 189–195.
- [7] R. Roldán, Y.E. Romanyuk, Dynamics in electrochromic windows interpreted with an extended logistic model, *J. Electrochem. Soc.* 163 (2016) E235–E240.
- [8] M. Casini, Smart windows for energy efficiency of buildings, *Int. J. Civ. Eng.* 2 (2016) 230–238.
- [9] A.L.-S. Eh, A.W.M. Tan, X. Cheng, S. Magdassi, P.S. Lee, Recent advances in flexible electrochromic devices: prerequisites, challenges, and prospects, *Energy Technol.* 5 (2017) 1–14.
- [10] X. Liu, A. Zhou, Y. Dou, T. Pan, M. Shao, J. Han, M. Wei, Ultrafast switching of an electrochromic device based on layered double hydroxide/prussian blue multi-layered films, *Nanoscale* 7 (2015) 17088–17095.
- [11] L. Zhu, C.K.N. Peh, T. Zhu, Y.-F. Lim, G.W. Ho, Bifunctional 2D-on-2D MoO_3 Nanobelt/ $\text{Ni}(\text{OH})_2$ nanosheets for supercapacitor-driven electrochromic energy storage, *J. Mater. Chem. A* 5 (2017) 8343–8351.
- [12] G. Yuan, C. Hua, L. Huang, C. Defranoux, P. Basa, Y. Liu, C. Song, G. Han, Optical characterization of the coloration process in electrochromic amorphous and crystalline WO_3 films by spectroscopic ellipsometry, *Appl. Surf. Sci.* 421 (2017) 630–635.
- [13] O. Arutanti, A.B.D. Nandiyanto, T. Ogi, T.O. Kim, K. Okuyama, Influences of porous structuration and Pt addition on the improvement of photocatalytic performance of WO_3 particles, *ACS. Appl. Mater. Interface* 7 (2015) 3009–3017.
- [14] G. Cai, M. Cui, V. Kumar, P. Darmawan, J. Wang, X. Wang, A.L.-S. Eh, K. Qian, P.S. Lee, Ultra-large optical modulation of electrochromic porous WO_3 film and the local monitoring of redox activity, *Chem. Sci.* 7 (2016) 1373–1382.
- [15] S.K. Deb, Opportunities and challenges in science and technology of WO_3 for electrochromic and related applications, *Sol. Energy Mater. Sol. Cells* 92 (2008) 245–258.
- [16] F. Zheng, W. Man, M. Guo, M. Zhang, Q. Zhen, Effects of morphology, size and crystallinity on the electrochromic properties of nanostructured WO_3 films, *CrystEngComm*. 17 (2015) 5440–5450.
- [17] S. Heo, J. Kim, G.K. Ong, D.J. Milliron, Template-free mesoporous electrochromic films on flexible substrates from tungsten oxide nanorods, *Nano Lett.* 17 (2017) 5756–5761.
- [18] J.Z. Ou, S. Balendhran, M.R. Field, D.G. McCulloch, A.S. Zoofakar, R.A. Rani, S. Zhuiykov, A.P. O'Mullane, K. Kalantar-zadeh, The anodized crystalline WO_3 nanoporous network with enhanced electrochromic properties, *Nanoscale* 4 (2012) 5980–5988.
- [19] S.R. Bathe, P.S. Patil, Electrochromic characteristics of fibrous reticulated WO_3 thin films prepared by pulsed spray pyrolysis technique, *Sol. Energy Mater. Sol. Cells* 91 (2007) 1097–1101.
- [20] X. Yang, G. Zhu, S. Wang, R. Zhang, L. Lin, W. Wu, Z.L. Wang, A self-powered electrochromic device driven by a nanogenerator, *Energy Environ. Sci.* 5 (2012) 9462–9466.
- [21] K. Gesheva, A. Szekers, T. Ivanova, Optical properties of chemical vapor deposited thin films of molybdenum and tungsten based metal oxides, *Sol. Energy Mater. Sol. Cells* 76 (2003) 563–576.
- [22] D. Ma, G. Shi, H. Wang, Q. Zhang, Y. Li, Morphology-tailored synthesis of vertically aligned 1D WO_3 nano-structure films for highly enhanced electrochromic performance, *J. Mater. Chem. A* 1 (2013) 684–691.
- [23] J.P. Cronin, D.J. Tarico, J.C.L. Tonazzi, A. Agrawal, S.R. Kennedy, Microstructure and properties of sol-gel deposited WO_3 coatings for large area electrochromic windows, *Sol. Energy Mater. Sol. Cells* 29 (1993) 371–386.
- [24] J. Zhou, Y. Wei, G. Luo, J. Zheng, C. Xu, Electrochromic properties of vertically aligned Ni-doped WO_3 nanostructure films and their application in complementary electrochromic devices, *J. Mater. Chem. C* 4 (2016) 1613–1622.
- [25] S.R. Bathe, P.S. Patil, Influence of Nb doping on the electrochromic properties of WO_3 films, *J. Phys. D: Appl. Phys.* 40 (2007) 1476–1486.
- [26] P. Porkodi, V. Yegnaraman, D. Jeyakumar, Polyol mediated synthesis of tungsten trioxide and Ti doped tungsten trioxide Part 1: synthesis and characterization of the precursor material, *Mater. Res. Bull.* 41 (2006) 1476–1486.
- [27] R.Y. Hong, H.P. Fu, G.Q. Di, Y. Zheng, D.G. Wei, Facile route to $\gamma\text{-Fe}_2\text{O}_3/\text{SiO}_2$ nanocomposite used as a precursor of magnetic fluid, *Mater. Chem. Phys.* 108 (2008) 132–141.
- [28] T. Tesfamichael, C. Piloto, M. Arita, J. Bell, Fabrication of Fe-doped WO_3 films for NO_2 sensing at lower operating temperature, *Sens. Actuator B-Chem.* 221 (2015) 393–400.
- [29] M. Caiado, A. Machado, R.N. Santos, I. Matos, I.M. Fonseca, A.M. Ramos, J. Vital, A.A. Valente, J.E. Castanheiro, Alkoxylation of camphene over silica-occluded tungstophosphoric acid, *Appl. Catal. A-Gen.* 451 (2013) 36–42.
- [30] M. Ahsan, T. Tesfamichael, M. Ionescu, J. Bell, N. Motta, Low temperature CO sensitive nanostructured WO_3 thin films doped with Fe, *Sens. Actuator B-Chem.* 162 (2012) 14–21.
- [31] D. Grosso, C. Boissière, B. Smarsly, T. Brezesinski, N. Pinna, P.A. Albouy, H. Amenitsch, M. Antonietti, C. Sanchez, Periodically ordered nanoscale islands and mesoporous films composed of nanocrystalline multimetallic oxides, *Nat. Mater.* 3 (2004) 787–792.
- [32] K.N. Tu, U. Gösele, Hollow nanostructures based on the kirckendall effect: design and stability considerations, *Appl. Phys. Lett.* 86 (2005) 093111.
- [33] B.-R. Koo, S.-T. Oh, H.-J. Ahn, Camphene effect for morphological change of electrospun SnO_2 nanofibres: from dense to fibre-in-hollow and to hollow nanostructures, *Mater. Lett.* 178 (2016) 288–291.
- [34] L. Yang, D. Ge, J. Zhao, Y. Ding, X. Kong, Y. Li, Improved electrochromic performance of ordered macroporous tungsten oxide films for IR electrochromic device, *Sol. Energy Mater. Sol. Cells* 100 (2012) 251–257.
- [35] L. Xiao, Y. Lv, W. Dong, N. Zhang, X. Liu, Dual-functional WO_3 nanocolumns with broadband antireflective and high-performance flexible electrochromic properties, *ACS. Appl. Mater. Interfaces* 40 (2016) 27107–27114.
- [36] H. Song, Y. Li, Z. Lou, M. Xiao, L. Hu, Z. Ye, L. Zhu, Synthesis of Fe-doped WO_3 nanostructures with high visible-light-driven photocatalytic activities, *Appl. Catal. B-Environ.* 166–167 (2015) 112–120.
- [37] S.-J. Yoon, A. Joshi, K. Uchino, Effect of additives on the electromechanical properties of $\text{Pb}(\text{Zr}, \text{Ti})\text{O}_3\text{-Pb}(\text{Y}_{2/3}\text{W}_{1/3})\text{O}_3$ ceramics, *J. Am. Ceram. Soc.* 80 (1997) 1035–1039.
- [38] T. Zhang, Z. Zhu, H. Chen, Y. Bai, S. Xiao, X. Zheng, Q. Xue, S. Yang, Iron-doping-enhanced photoelectrochemical water splitting performance of nanostructured WO_3 : a combined experimental and theoretical study, *Nanoscale* 7 (2015) 2933–2940.
- [39] K. Mašek, P. Biumentrit, J. Beran, T. Skála, I. Píš, J. Libra, V. Matolín, Pt-doped tungsten oxide surface: photoemission and RHEED study, *Surf. Interface Anal.* 42 (2010) 540–544.
- [40] B.V. Lvov, A.A. Vasilevich, A.O. Dyakov, J.W.H. Lam, R.E. Sturgeon, Reduction of metal oxides by carbon in graphite furnaces Part 1. Temporal oscillations of atomic absorption in the process of slow evaporation of Al, Bi, Cr, In, Mg, Mn, Pb, Sb, Sn and Te oxides, *J. Anal. At. Spectrom.* 14 (1999) 1019–1024.
- [41] M. Barawi, L.D. Trizio, R. Giannuzzi, G. Veramonti, L. Manna, M. Manca, Dual band electrochromic devices based on Nb-Doped TiO_2 nanocrystalline electrodes, *ACS. Nano* 11 (2017) 3576–3584.
- [42] L. Vayssieres, C. Sathe, S.M. Butorin, D.K. Shuh, J. Nordgren, J. Guo, One-dimensional quantum-confinement effect in $\alpha\text{-Fe}_2\text{O}_3$ ultrafine nanorod arrays, *Adv. Mater.* 17 (2005) 2320–2323.
- [43] V. Etacheri, R. Roshan, V. Kumar, Mg-Doped ZnO nanoparticles for efficient sunlight-driven photocatalysis, *ACS. Appl. Mater. Interfaces* 4 (2012) 2717–2725.
- [44] B.E. Sernelius, K.-F. Berggren, Z.-C. Jin, I. Hamberg, C.G. Granqvist, Band-gap tailoring of ZnO by means of heavy Al doping, *Phys. Rev. B* 37 (1988) 10244–10248.
- [45] W. Dong, Y. Lv, L. Xiao, Y. Fan, N. Zhang, X. Liu, Bifunctional $\text{MoO}_3\text{-WO}_3/\text{Ag}/\text{MoO}_3\text{-WO}_3$ films for efficient ITO-free electrochromic devices, *ACS. Appl. Mater. Interfaces* 8 (2016) 33842–33847.
- [46] G. Luo, L. Shen, J. Zheng, C. Xu, Europium ions doped WO_3 film with bi-function of enhanced electrochromic switching and tunable red emission, *J. Mater. Chem. C* 5 (2017) 3488–3494.
- [47] X. Liu, A. Zhou, Y. Dou, T. Pan, M. Shao, J. Han, M. Wei, Ultrafast switching of an electrochromic device based on layered double hydroxide/prussian blue multi-layered films, *Nanoscale* 7 (2015) 17088–17095.
- [48] A. Zhou, X. Liu, Y. Dou, S. Guan, J. Han, M. Wei, The fabrication of oriented organic-inorganic ultrathin films with enhanced electrochromic properties, *J. Mater. Chem. C* 4 (2016) 8284–8290.